Research Article Vol. 28, No. 1 / 6 January 2020 / Optics Express 71
Optics EXPRESS

Demonstration of a combined differential absorption and high spectral resolution lidar for profiling atmospheric temperature

ROBERT A. STILLWELL,[1,2,*] SCOTT M. SPULER,[2] MATTHEW HAYMAN,[2] KEVIN S. REPASKY,[2,3,4] AND CATHARINE E. BUNN[4]

[1]*Advanced Study Program, National Center for Atmospheric Research, 3450 Mitchell Lane, Bldg 1, CO 80301, USA*
[2]*Earth Observing Laboratory, National Center for Atmospheric Research, 3450 Mitchell Lane, Bldg 1, CO 80301, USA*
[3]*Electrical and Computer Engineering, Montana State University, Bozeman, MT 59717-2660, USA*
[4]*Physics Department, Montana State University, Bozeman, MT 59717-2660, USA*
[*]*robert.stillwell@colorado.edu*

Abstract: This work presents the first demonstration of atmospheric temperature measurement using the differential absorption lidar (DIAL) technique. While DIAL is routinely used to measure atmospheric gases such as ozone and water vapor, almost no success has been found in using DIAL to measure atmospheric temperature. Attempts to measure temperature using a well-mixed gas like oxygen (O_2) have largely failed based on a need for quantitative ancillary measurements of water vapor and atmospheric aerosols. Here, a lidar is described and demonstrated that simultaneously measures O_2 absorption, water vapor number density, and aerosol backscatter ratio. This combination of measurements allows for the first measurements of atmospheric temperature with useful accuracy. DIAL temperature measurements are presented to an altitude of 4 *km* with 225 *m* and 30 *min* resolution with accuracy better than 3 *K*. DIAL temperature data is compared to a co-located Raman lidar system and radiosondes to evaluate the system's performance. Finally, an analysis of current performance characteristics is presented, which highlights pathways for future improvement of this proof-of-concept instrument.

1. Introduction

Ground-based profiling of atmospheric water vapor mixing ratio and temperature in the troposphere is of great importance to the skill of numerical weather prediction models for severe weather forecasting. Despite their importance, ground-based profiles of thermodynamic variables have been identified as a major observational gap in the current observational system [1–4]. Specific deficiencies have been clearly identified by the National Research Council in both spatial and temporal resolution of tropospheric thermodynamic variables [1]. While several instruments and techniques are available to help address these deficiencies and close this observational gap, including both active and passive remote sensing technologies, lidar systems have been identified for their potential to address most of the tropospheric thermodynamic gap currently noted [3].

To date, Raman lidar systems leveraging inelastic Raman scattering [5–10] are the only active optical remote sensing tool that can provide full thermodynamic profiling of the lower troposphere. These systems can measure water vapor mixing ratio using the vibrational Raman technique [11–18] and atmospheric temperature using the rotational Raman technique [17–23]. The theoretical simplicity of the Raman lidar technique is attractive, but the practical implementations of Raman systems can be complex. Additionally, the inefficient nature of Raman scattering necessitates the use of designs with high power/aperture products. This results in systems with lasers that have high peak-power making unattended operation and eye safety a considerable

#379804 https://doi.org/10.1364/OE.379804
Journal © 2020 Received 9 Oct 2019; revised 11 Dec 2019; accepted 12 Dec 2019; published 23 Dec 2019

Optics EXPRESS

challenge. Currently, to our knowledge, four Raman lidar systems worldwide (the Caeli lidar operated by the Royal Netherlands Meteorological Institute [12], the RALMO system operated by Meteo Swiss [15,16], the Raman lidar system operated by the Atmospheric Radiation Measurement Program [17], and the RAMSES system operated by the Deutsche Wetterdienst [18]) have been shown to operate in the autonomous and unattended fashion required for operational applications, but none are designed for network deployment. Additionally, significant initial and maintenance costs are associated with the use of high peak-power lasers. Finally, while some attempts have been made to develop calibration methods for Raman lidar systems without ancillary measurements [24–26], in practical operation they rely on calibration from secondary measurements such as radiosondes. These inherent features of Raman lidar systems, i.e. eye-safety concerns, requirement for frequent calibration and maintenance, and high costs, are all contributing factors that make network deployment a significant challenge.

In contrast to Raman lidar systems, differential absorption lidar (DIAL) systems can leverage more efficient elastic scattering [5,27–30]. As elastic scattering is several orders of magnitude more efficient than inelastic Raman scattering, it significantly alleviates the requirement for high power/aperture product systems. This efficiency allows the use of commercially available, low-cost, robust, low-power semiconductor-based micropulse laser systems, especially in the lower troposphere where aerosol loading enhances the backscatter signal. DIAL generally has less flexibility in operational wavelength – defined by the species' absorption spectra – and typically requires a laser with narrow linewidth and high frequency stability, but the micropulse architecture with semiconductor lasers meets these requirements, and permits eye-safe designs (Class 1 or 1M transmitters) that show promise for both long-term unattended operation and network deployment. Additionally, narrowband DIAL systems do not require ancillary atmospheric observations, e.g. radiosondes, to calibrate the observations. Finally, DIAL has proven capable and reliable at measuring water vapor number density [31–38]. However, despite these advantages, DIAL has previously been unable to provide full thermodynamic profiling, lacking measurements of temperature.

The work of Theopold and Bösenberg [39–41] demonstrates that measurement of atmospheric temperature using DIAL is theoretically possible using temperature-sensitive absorption by oxygen (O_2). However, practical limitations have thus far prevented a viable demonstration of such a system with useful accuracy. The specific challenge is the unknown composition of the backscattered spectrum. The spectrum of light scattered from aerosols, assuming a narrowband transmitter, is nearly identical to the laser linewidth (on the order of a few MHz), but scattering from molecules produces a broad spectral component with a width comparable to the absorption line itself (on the order of 1 GHz). As a result, DIAL-based temperature measurements are sensitive to backscatter ratio, or the ratio of total scattering (combined aerosol and molecular scattering) to molecular scattering. Therefore, without an ability to measure the two components of the backscattered spectrum, early attempts to measure atmospheric temperature using DIAL resulted in errors on the order of 10 K [40]. Thus it has generally been assumed that DIAL systems are incapable of measuring high quality atmospheric temperature profiles.

Here a diode-laser-based micropulse DIAL system is introduced and demonstrated that is capable of measuring atmospheric temperature. It achieves this capability using a combination of DIAL and high spectral resolution lidar (HSRL) techniques. The system measures the water vapor number density, the backscatter ratio of the atmospheric signals, and the temperature-sensitive absorption of O_2. This work describes this system in detail and is organized as follows. Section 2 describes the theoretical and practical issues associated with making DIAL measurements of temperature. Section 3 describes the hardware design of the system capable of addressing these theoretical and practical issues. Section 4 presents the relevant theory to make atmospheric temperature measurements with the given design. Section 5 illustrates the first DIAL measurements of atmospheric temperature. Finally, Section 6 provides analysis of these

Optics EXPRESS

first measurements and an outlook on future development of the DIAL atmospheric temperature measurements.

2. Theoretical problem statement and novel solution

The work of Theopold and Bösenberg highlights that measurement of atmospheric temperature using DIAL requires both high-quality absorption measurements of O_2 and high-quality ancillary measurements, including quantitative measurements of water vapor number density and backscatter ratio [39–41]. This requirement can be clarified by defining a frequency resolved lidar equation, given in Eq. (1), similar to Eq. (1) from [40].

$$N_{R_x}^{\lambda}(\nu,R) = N_{T_x}^{\lambda}\Delta R\frac{A}{R^2}\eta_{T_x}^{\lambda}O^{\lambda}(R)\times \int_{-\infty}^{\infty}\left[l^{\lambda}(\nu)\,T^{\lambda}(\nu,R) * \beta^{\lambda}(\nu,R)\right]T^{\lambda}(\nu,R)\,\eta_{R_x}^{\lambda}(\nu)\,d\nu + B^{\lambda}(\nu) \tag{1}$$

Here the number of photons received $\left(N_{R_x}\right)$ is a function of frequency (ν), and range (R) as well as the transmitted number of photons $\left(N_{T_x}\right)$, the receiver range resolution (ΔR), telescope collecting area (A), transmitter and receiver optical efficiencies $\left(\eta_{T_x}\ and\ \eta_{R_x}\right)$, respectively, geometric overlap function (O), the normalized transmitted laser spectrum (l), atmospheric transmission (T), backscatter coefficient (β), and background noise (B). The scattering process is represented by a convolution operation in the spectral domain $(*)$ and the terms that will vary depending on the laser channel used are denoted by the superscript (λ). Note that $\int_{-\infty}^{\infty} l(\nu)d\nu = 1$ and describes the laser spectrum shape, not its magnitude. The magnitude is described by $N_{T_x}^{\lambda}\eta_{T_x}^{\lambda}$.

This equation is similar to standard lidar equations, e.g. presented in [41–43], with the exception that Eq. (1) does not assume the laser spectrum is unchanged from emission to collection. While assuming the laser spectrum is unchanged simplifies most lidar applications and does not result in a loss of generality, it is not applicable in some cases using narrowband DIAL. Simply stated, if the transmit and received spectra of light are not the same, here possibly modified by the scattering process, the lidar signal will be absorbed differently before and after scattering. This can affect measurements that leverage absorption processes, like narrowband DIAL.

Equation (1) can be recast to highlight the measurements required to retrieve temperature using DIAL. The following changes are made and given in Eq. (2).

1. A transmitted laser spectrum is assumed to be a delta function with emission frequency ν_{λ} $\left(l^{\lambda}(\nu) = \delta(\nu - \nu_{\lambda})\right)$.

2. Scattering by aerosols and molecules are explicitly split. Scattering from aerosols displaying almost no spectral broadening (in the case of a narrowband laser spectrum with a width of a few *MHz*, the scattering remains narrow), whereas scattering from molecules is broadened (on the order of a few *GHz*).

3. Backscatter ratio is defined as $BR^{\lambda}(R) = \frac{\beta_{Aer}^{\lambda}(\nu,R)+\beta_{Mol}^{\lambda}(\nu,R)}{\beta_{Mol}^{\lambda}(\nu,R)}$ where $\beta_{Aer}^{\lambda}(\nu,R)$ and $\beta_{Mol}^{\lambda}(\nu,R)$ are the backscattering coefficient of aerosols and molecules, respectively.

4. β_{Mol}^{λ} is split into a spectral shape $(\tilde{\beta}_m(\nu,R))$ and range dependent scaling factor $(\beta_m^{\lambda}(R))$ such that $\beta_{Mol}^{\lambda}(\nu,R) = \beta_m^{\lambda}(R)\,\tilde{\beta}_m(\nu,R)$. Note that $\int_{-\infty}^{\infty}\tilde{\beta}_m(\nu,R)d\nu = 1$ and simply describes the molecular spectrum shape, not its magnitude,

5. Normalized photon counts received are defined as $N^{\lambda}(R) = \frac{N_{R_x}^{\lambda}(\nu,R)-B^{\lambda}(\nu)}{N_{T_x}^{\lambda}}$.

Optics EXPRESS

$$N^{\lambda}(R) = \Delta R \frac{A}{R^2} \eta_{T_x}^{\lambda} \eta_{R_x}^{\lambda}(\nu_{\lambda}) O^{\lambda}(R) T^{\lambda 2}(\nu_{\lambda}, R) \beta_m^{\lambda}(R) \times \left\{ \left[BR^{\lambda}(R) - 1 \right] + \int_{-\infty}^{\infty} \tilde{\beta}_m(\nu - \nu_{\lambda}, R) \frac{T^{\lambda}(\nu, R)}{T^{\lambda}(\nu_{\lambda}, R)} \frac{\eta_{R_x}(\nu)}{\eta_{R_x}(\nu_{\lambda})} d\nu \right\} \tag{2}$$

There are two key backscatter terms in the brackets of Eq. (2), the first being the signal obtained from aerosol scatterers ($BR^{\lambda}(R) - 1$) and the second from molecular scatterers $\left(\int_{-\infty}^{\infty} \tilde{\beta}_m(\nu - \nu_{\lambda}, R) \frac{T^{\lambda}(\nu,R)}{T^{\lambda}(\nu_{\lambda},R)} \frac{\eta_{R_x}(\nu)}{\eta_{R_x}(\nu_{\lambda})} d\nu \right)$. For cases where the laser spectrum is narrow and the molecular backscatter is broad relative to the absorption feature of interest (as will be the case for narrowband O_2 DIAL leveraging scattering off of molecules and aerosols), a difference in the absorption of light scattered by aerosol and scattered by molecules is clear. It is therefore necessary to know the relative amount of aerosol and molecular backscatter in a collected return as described by $BR^{\lambda}(R)$ to invert Eq. (2).

One subtle point to be made is that most DIAL systems, for example measuring water vapor or ozone, seek to measure the absorption coefficient (embedded within the $T^{\lambda}(\nu, R)$ terms). This absorption coefficient is a function of temperature, pressure (combined affecting the absorption cross-section), and the number density of the absorber. By leveraging a temperature-insensitive absorption line, a direct relation is forced between the absorption coefficient (the measured quantity) and the number density of a species (the desired quantity). However, in this case, the measured quantity is still absorption but the desired quantity is temperature. Temperature is retrievable but number density must be known. The use of a well mixed species like O_2 is the basis for the technique, but the number density can change. Specifically, the number density of water vapor alters the mixing ratio of O_2 [44].

In summary, to invert Eq. (2) for temperature, three measurements are needed. First, the mixing ratio of an absorbing gas is required. Using atmospheric O_2 as the absorbing gas, the main gas that can alter the mixing ratio is water vapor. Therefore, the water vapor number density must be measured. Second, the backscatter ratio is required to separate the absorption of light after scattering by aerosols and molecules. Third, the temperature-sensitive absorption coefficient must be measured. These three pieces of information are used to ultimately retrieve temperature.

The practical solution provided in this work to measure temperature is therefore a combined DIAL and HSRL system. This system uses one DIAL wavelength pair to measure water vapor, an HSRL to measure backscatter ratio, and a second DIAL pair to measure O_2 absorption. This solution is fundamentally different to both the high resolution DIAL approach proposed by Bösenberg [40] and the broadband emission approach, referred to as BELINDA, (described in Chapter 14 of Weitkamp et al. [41]) where in both cases efforts are made to minimize the impact of molecular broadening. In contrast, we aim to measure the effect itself and analyze observations by including this additional information.

The work of Theopold and Bösenberg, attempting broadly the same measurement principle as that proposed here, showed major errors in temperature measurements using narrowband DIAL largely because they lacked quantitative measurements of backscatter ratio. They attempted to estimate backscatter ratio using a Klett/Fernald type inversion [45,46]. Furthermore, at the time of writing, creating a laser transmitter capable of making all the measurements needed for such a sensor was prohibitively complex [47]. This led to the widely held assumption that DIAL systems can not measure temperature. Today, however, the advent of diode-laser-based lidar systems have made the development of spectrally agile, robust, low-cost, and modular laser transmitters possible. This technology enables measurements of water vapor number density [34–37] and backscatter ratio [48] with sufficient accuracy to warrant the reevaluation of the assumption that DIAL systems cannot provide accurate temperature measurements.

Optics EXPRESS

3. MicroPulse DIAL hardware

The diode-laser-based architecture we have developed is referred to as MicroPulse DIAL (MPD). The details of measurement hardware, theory, and retrievals of each individual system are described here only where they deviate from the previously-described DIAL [36,37] and HSRL [48] techniques. The MPD hardware is discussed here and the measurement theory is discussed in Section 4.

The temperature MPD transmits four laser wavelengths and has three detectors, a block diagram of the architecture is shown in Fig. 1 with specifications listed in Table 1. A single pair of transmit wavelengths near 828 *nm*, approximately 828.195 *nm* for the water vapor online and 828.295 *nm* for the water vapor offline, is used to measure water vapor number density using the standard DIAL technique [31,49]. Note that these wavelengths are approximate as they can be tuned to accommodate greater or lesser absorption, by moving the online wavelength's position up or down the water vapor side line, corresponding to drier or moister environments. This feature is only needed for water vapor measurements since water vapor is highly variable in the atmosphere. The two wavelengths are combined using fiber-coupled opto-electric switches and used to seed a single tapered semiconductor optical amplifier (TSOA). This signal is both transmitted and received by a shared telescope design where the inner telescope area is used as the transmit reflector and the outer telescope area used for collecting backscattered light. The collected backscattered light is directed into a multi-mode fiber and coupled into the receiver module. Narrowband filtering in this module is provided by two interference filters with full-width at half maximum (FWHM) of approximately 0.5 *nm*, and a solid fused silica etalon with a FWHM fringe pass-band of approximately 2×10^{-3} *nm* (1 *GHz*). The etalon is designed to pass both on and offline wavelengths of light from the transmitter in adjacent cavity modes, with a free spectral range of about 0.1 *nm* (44 *GHz*). Both wavelengths of light are collected on a common detector [36]. The performance of water vapor retrievals from this system architecture was validated by Weckwerth et al. [37]. This base water vapor DIAL system is modified by adding a second DIAL wavelength pair near 770 *nm* to measure O_2 absorption. Dichroic filters combine the water vapor and O_2 wavelengths into a common transmit beam and and split the water vapor and O_2 wavelengths in the receiver. The additional O_2 DIAL elements are shown in red in Fig. 1. An additional detector with a narrowband notch filter is also added to the O_2 DIAL receiver to implement the HSRL technique. This is shown in pink in Fig. 1.

Table 1. Specifications for the combined O_2 DIAL and HSRL system presented in Fig. 1. Specifications for the water vapor DIAL pair can be found in Spuler et al. Table 1 [36]. Abbreviations used are: FSR = free spectral range and NBF = narrow band filter.

Transmitter	Specification	Receiver	Specification
Wavelength	769.7958 *nm* (online)	Etalon Finesse	15.43
	770.1085 *nm* (offline)	Etalon FSR	157.90 *GHz*
Output Power	30 *mW* (combined)	NBF Bandwidth	13 *nm*, 1 *nm*
Linewidth	<1 *MHz*	NBF out-of-band blocking	10^{-6}, 10^{-4}
Locking Tolerance	5×10^{-5} *nm*	NBF transmission	90%, 70%
Spectral Purity	99.9%	Potassium cell length	72 *mm*
Repetition Rate	7 *kHz* (combined)	Potassium cell temperature	378 *K*

A pair of wavelengths at 769.7958 *nm* (online) and 770.1085 *nm* (offline) are used to measure the temperature-sensitive O_2 absorption. Except for the difference in wavelength, the laser transmitter design is the same as the water vapor system. Common timing sources are used for the water vapor and O_2 lasers, i.e. the online(offline) lasers for water vapor and O_2 fire at the same time with the same duration.

Optics EXPRESS

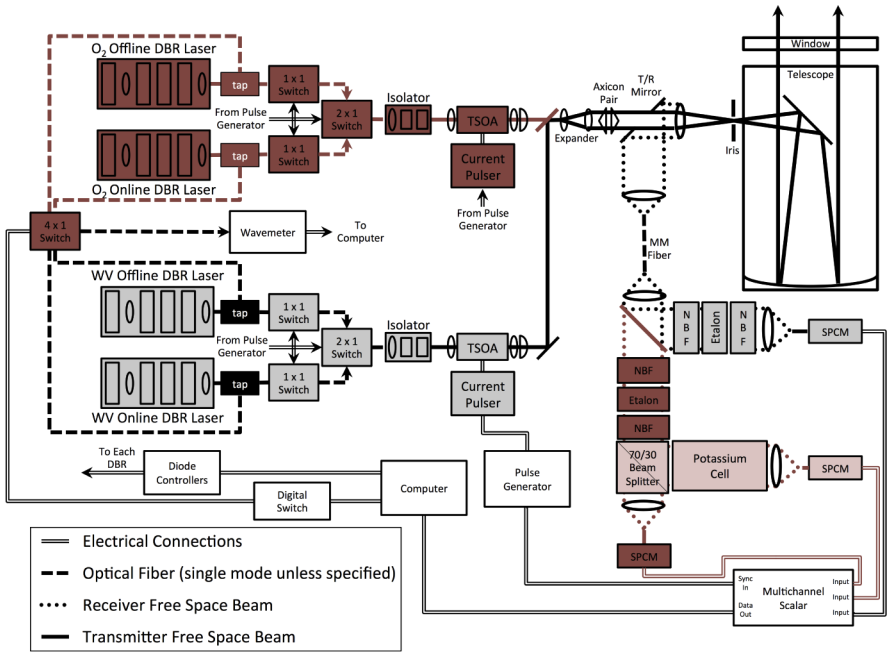

Fig. 1. A block diagram of the NCAR MPD system combining DIAL and HSRL techniques to measure water vapor, aerosol properties, and temperature-sensitive absorption. Abbreviations used are: Distributed Bragg Reflector (DBR), Multi-Mode (MM), Narrow Band Filter (NBF), Single Photon Counting Modules (SPCM), Tapered Semiconductor Optical Amplifier (TSOA), and Transmit/Receive (T/R).

Quantitative aerosol measurements are obtained with the HSRL technique based on a potassium vapor cell providing the narrowband blocking filter. The HSRL technique as described in Piironen and Eloranta, uses a narrowband blocking filter to remove the aerosol backscatter component yet pass some of the broader molecular backscattered light in one channel, which is referenced against another channel that contains the total backscatter, thus providing a method to quantitatively measure the backscatter ratio [50]. The exact amount of light transmitted in each channel can be calibrated and is referred to in Step 0 of Table 2 and Appendix A. The system was designed so the O_2 offline wavelength corresponds to the D_1 line of the potassium absorption spectrum (KD_1). The O_2 offline channel serves two purposes. It is both a reference for the O_2 online absorption and the transmit wavelength used for the HSRL measurement, i.e. the O_2 offline is, in effect, required to be a calibrated reference, as opposed to the water vapor offline channel, which is an uncalibrated (or floating) reference. This dual purpose reference enables quantitative measurement of aerosol scattering with the O_2 offline signal in contrast to the qualitative information described by Bösenberg using a Klett/Fernald type inversion [40,45,46]. This added capability provides the high quality ancillary aerosol data required and simultaneously simplifies the system compared to designs we previously considered where the O_2 DIAL and HSRL would be completely independent, for example using an HSRL based on the D_2 line of rubidium-87 (RbD_2) [48]. An additional benefit of selecting the KD_1 HSRL is that the aerosol optical properties are measured at the relevant wavelength and do not require conversion using an assumed angstrom exponent as vibrational Raman lidar retrievals require, e.g. [51]. Finally, the HSRL system is a convenient way to monitor the output laser's spectral purity, which is one of the more critical laser specifications, as described by Wulfmeyer [47].

Optics EXPRESS

Table 2. Processing steps to retrieve atmospheric temperature profiles from DIAL and HSRL measurements.

#	Processing Step	Details
0	Perform HSRL receiver calibration at instrument setup	See Appendix A
1	Assume initial temperature and pressure profile	
2	Calculate water vapor absorption cross sections	See [54]
3	Calculate water vapor number density from online and offline photon count measurements	See [36]
4	Calculate backscatter ratio from combined and molecular photon count measurements	Eq. (6)
5	Perform perturbative retrieval on O_2 DIAL data	See [55] and [56]
6	Perform iterative retrieval to retrieve temperature	See Eq. (8) and [44]

One additional benefit of this design is the availability of calibration information. Using the same technique as presented for the water vapor channel, where the DIAL wavelength pairs share an optical path through the transmitter and receiver, allows for HSRL calibration information related to geometric overlap and detector sensitivity to be easily retrieved without needing to run dedicated calibration scans. In this case, the offline wavelength serves as the HSRL wavelength while the online serves as a co-aligned calibration reference as it passes the KD_1 filter without significant attenuation. A measured spectrum of the etalon as well as the relevant section of the O_2 A-band and KD_1 line is given in Fig. 2.

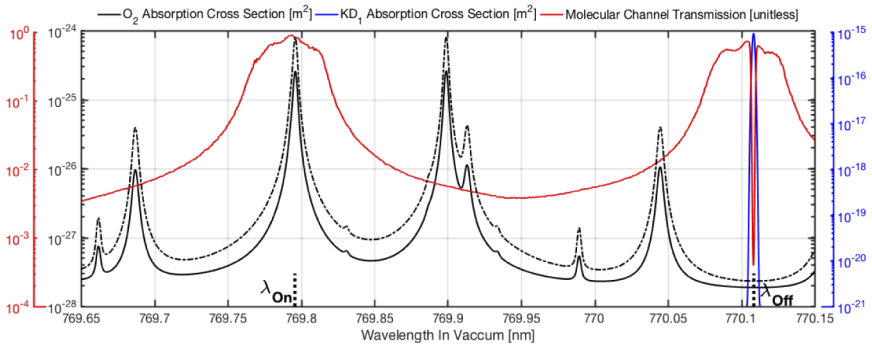

Fig. 2. A section of the calculated O_2 A-band absorption spectrum with the calculated KD_1 absorption spectrum and measured receiver transmission spectrum of the molecular channel. The O_2 absorption cross section is taken at 300 K for the dashed line and 250 K for the solid line. The combined channel absorption spectrum is identical to the molecular channel with the exception of the KD_1 absorption trough. The online wavelength, indicated as λ_{On}, is chosen at the line center of the 769.7958 *nm* O_2 absorption line and the offline wavelength, indicated as λ_{Off}, is chosen at the line center of the KD_1 line at 770.1085 *nm*. Parameters for calculating $O_2(KD_1)$ absorption are taken from Hitran 2012(von Zahn and Hoeffner 1996) [52,53].

4. Measurement theory

A general overview of the processing steps to arrive at temperature measurements is given in Table 2. Temperature and pressure profiles are needed for both water vapor number density and HSRL retrievals, but both retrievals are relatively insensitive to these parameters, by design. Therefore, as a first step, a hydrostatic atmosphere and constant lapse rate are assumed starting

Optics EXPRESS

with measurements from a surface weather station. With these profiles, water vapor number density and backscatter ratio are retrieved. The true atmospheric temperature can then be retrieved using a perturbative retrieval to obtain the absorption coefficient of O_2 then an iterative retrieval to obtain temperature from the retrieved O_2 absorption coefficient. These major steps are further described here.

4.1. Water vapor measurements

The retrieval of water vapor number density from MPD measurements follows the development of Spuler et al. [36]. A weather station (Lufft Smart Weather Sensor WS300) is present on the instrument to provide surface temperature and pressure. A constant lapse rate of $-9.8\ K/km$ was assumed for this analysis. Water vapor absorption spectra were calculated from Hitran 2012 parameterizations [52], which were then used to train a principle component analysis to calculate spectra at all range bins and time steps following Hayman et al. [54]. No other modifications to the retrieval methodology of Spuler et al. were made. Data is of best quality from approximately 450 m to 4-5 km [36,37].

4.2. High spectral resolution retrievals

The HSRL system used for this demonstration is based on a natural abundance potassium vapor cell. The use of potassium as opposed to previously described iodine or rubidium HSRL systems allows for advantages in terms of system calibration and hardware simplicity. The O_2 online laser passes through the system on exactly the same optical path as the O_2 offline laser without being attenuated by the KD_1 filter. This provides a method to retrieve calibration information related to the overlap and differential sensitivity of the two HSRL detectors. Additionally, all aerosol parameters are measured sufficiently near the O_2 absorption line that conversions are not required, such as an Angstrom exponent conversion in vibrational Raman lidar retrievals (e.g. [51]).

All HSRL parameters can be described using the lidar equation given in Eq. (1). For simplicity, the background subtracted observed counts for a particular laser wavelength and detector will be defined as $N_{R_x}{}^{Laser}_{Detector}(\nu, R) - B^{Laser}_{Detector}(\nu) = N^{Laser}_{Detector}$. The notation indicating the explicit dependency of the photon counts on frequency and range will be dropped henceforth.

The first major advantage of the KD_1 HSRL is that calibration parameters for differential detector sensitivity and differential overlap function of the two HSRL parameters can be measured directly using the O_2 online channel. The O_2 online data passes through an adjacent etalon cavity mode as the O_2 offline data and is only 0.3 nm separated in wavelength from the O_2 offline wavelength. As such, all atmospheric scattering, extinction, and optical system effects are effectively the same. Using Eq. (1) and taking the ratio of the O_2 online counts observed on the combined (detector leg without the potassium vapor cell) and molecular (detector leg with the potassium vapor cell) detectors and canceling common terms yields the combined detector sensitivity and differential geometric overlap function directly, as shown in Eq. (3).

$$\frac{N^{O_2On}_{Comb}}{N^{O_2On}_{Mol}} = \frac{\eta^{O_2On}_{Comb}(\nu)\, O^{O_2On}_{Comb}(R)}{\eta^{O_2On}_{Mol}(\nu)\, O^{O_2On}_{Mol}(R)}. \tag{3}$$

Note that the data in Eq. (3) can either be retrieved as a calibration of the measurement, i.e in advance using long integration time to reduce the shot-noise error, or during the measurement of interest, i.e. measure all online calibration data at the same time as the HSRL measurements. Either are valid calibration methods.

To retrieve the backscatter ratio the O_2 offline data are used. In a similar manner to the O_2 online measurements, the ratio of the offline signals is used. The primary difference is that the scattering cross section does not cancel as the potassium vapor cell attenuates the light

Optics EXPRESS

scattered primarily by aerosols. Additionally, the etalon and potassium vapor cell can attenuate the molecular backscatter. To account for non-equal system efficiencies, 4 calibration parameters are introduced. An equation of the form of Eq. (4) can be created with specific system efficiencies C_{ij}. Here i is either M or A corresponding to molecular backscatter and aerosol backscatter, respectively, and j is either C or M corresponding to combined or molecular channels, respectively. The term η is shorthand for all other terms of Eq. (1) corresponding to either the combined or molecular channels excluding the backscatter terms.

$$\begin{bmatrix} N_{Comb}^{O_2Off} \\ N_{Mol}^{O_2Off} \end{bmatrix} = \begin{bmatrix} \eta_C & 0 \\ 0 & \eta_M \end{bmatrix} \begin{bmatrix} C_{MC} & C_{AC} \\ C_{MM} & C_{AM} \end{bmatrix} \begin{bmatrix} \beta_{Mol}^{O_2Off}(\nu, R) \\ \beta_{Aer}^{O_2Off}(\nu, R) \end{bmatrix} \tag{4}$$

These calibration parameters are determined by scanning the output laser wavelength measured by the receiver to map the receiver efficiency as a function of wavelength. C_{AC} is normalized to 1 where its effect is captured by the $\eta_{R_x}^{\lambda}(\nu)$ term of Eq. (1). These data are shown as the red line in Fig. 2 and result in the following approximate calibration coefficients: $C_{MC} \approx 0.92$, $C_{MM} \approx 0.2$, and $C_{AM} \approx 0.0005$. More information on this procedure is given in Appendix A. With the KD_1 HSRL general photon counts defined in Eq. (4), taking the ratio of the O_2 offline counts observed on the combined and molecular detectors yields:

$$\frac{N_{Comb}^{O_2Off}}{N_{Mol}^{O_2Off}} = \left[\frac{\eta_{Comb}^{O_2Off}(\nu)\, O_{Comb}^{O_2Off}(R)}{\eta_{Mol}^{O_2Off}(\nu)\, O_{Mol}^{O_2Off}(R)}\right] \left[\frac{C_{MC}\beta_{Mol}^{O_2Off}(\nu, R) + \beta_{Aer}^{O_2Off}(\nu, R)}{C_{MM}\beta_{Mol}^{O_2Off}(\nu, R) + C_{AM}\beta_{Aer}^{O_2Off}(\nu, R)}\right] \tag{5}$$

By design, the efficiencies of the optical system to both lasers are the same, i.e. $\eta_{Comb}^{O_2On}(\nu) = \eta_{Comb}^{O_2Off}(\nu)$ and $\eta_{Mol}^{O_2On}(\nu) = \eta_{Mol}^{O_2Off}(\nu)$ (excluding the effects of the absorption of the potassium vapor cell on the molecular spectrum, which is captured by the C_{MM} term). Additionally, given that the lasers originate from the same amplifier, the overlap function for each laser on the same detectors are equivalent. Therefore, by design $O_{Mol}^{O_2On}(R) = O_{Mol}^{O_2Off}(R)$ and $O_{Comb}^{O_2On}(R) = O_{Comb}^{O_2Off}(R)$. Inserting all of these equivalent values into Eq. (3) and inserting that into Eq. (5) yields an expression for the aerosol backscatter component as a function of measured photon counts and the molecular scatter component. With this explicit definition of the aerosol component, the backscatter ratio can be expressed only in terms of observed photon counts and determined calibration constants, C_{MM}, C_{MC} and C_{AM} as given in Eq. (6).

$$BR = \frac{\beta_{Aer}^{O_2Off} + \beta_{Mol}^{O_2Off}}{\beta_{Mol}^{O_2Off}} = 1 - \left\{\frac{C_{MM}\left[N_{Comb}^{O_2Off} N_{Mol}^{O_2On}\right] - C_{MC}\left[N_{Mol}^{O_2Off} N_{Comb}^{O_2On}\right]}{C_{AM}\left[N_{Comb}^{O_2Off} N_{Mol}^{O_2On}\right] - \left[N_{Mol}^{O_2Off} N_{Comb}^{O_2On}\right]}\right\} \tag{6}$$

4.3. Temperature retrievals

Previous attempts to measure temperature have been based on the DIAL technique using a specific O_2 absorption line within the A-band. The major source of error identified was the unknown relative composition of aerosol and molecular scattering at each altitude of the atmosphere (expressed by the backscatter ratio). Attempts using a Fernald [45] or Klett [46] inversion to retrieve backscatter ratio were unsuccessful. These inversions require assumptions about the backscatter-to-extinction ratio and generally perform poorly without large extinction, making them poorly suited for regions of variable aerosol loading, the primary region of interest for this data product. As a direct result of the lack of high quality co-located measurements of water vapor and backscatter ratio, large errors on the order of 10 K were observed [40]. However, the above described DIAL/HSRL alleviates such concern in 3 distinct ways. First, the backscatter ratio is measured directly with an HSRL system, whereas a lidar ratio must be assumed, often

Optics EXPRESS

with large uncertainty, for both the Fernald or Klett inversion to retrieve backscatter ratio. Second, HSRL observations are well behaved for low backscatter ratio scenes (e.g. $BR \leq 1-10$) while Fernald or Klett inversions are less so as HSRL measurements are based directly on measured signal levels and not based on derivatives of the same. In addition, water vapor number density is also required for the temperature retrieval, and while this measurement capability has existed within the DIAL architecture for some time, the MPD design makes integration of all three observations relatively simple so that the observation is directly measured in common volume with the O_2 DIAL.

Because the integral term in Eq. (1) cannot be ignored in the O_2 DIAL equation, the standard DIAL equation cannot be used to solve for the oxygen absorption coefficient. Even though we are able to obtain the backscatter ratio through the HSRL channels and water vapor from the water vapor DIAL channels, there is no analytical solution for the difference in oxygen absorption between the two channels, and therefore the temperature profile. Obtaining temperature from O_2 DIAL observations inherently requires a numerical solver. In this work we use a perturbative solution to the 2-component DIAL equation described by Bunn et al. and Repasky et al. [55,56] where the effect of Rayleigh-Doppler broadening on the absorption coefficient is corrected by applying 1^{st} and 2^{nd} order perturbative terms to the original 0^{th} order retrieval. The retrieved absorption coefficient is then converted to temperature using an iterative method as described by Korb and Weng [44]. Specifically, Korb and Weng define the temperature dependence of the absorption coefficient as given in Eq. (7).

$$\alpha_{O_2} = q_{O_2}\left[1 - q_{H_2O}\right]\frac{P}{k_B T} S_o \frac{T_o}{T} \exp\left\{-\frac{\epsilon hc}{k_B}\left[\frac{1}{T} - \frac{1}{T_o}\right]\right\}\Lambda\left(\nu, T\right), \tag{7}$$

where the absorption coefficient $\left(\alpha_{O_2}\right)$ is a function of the mixing ratios of oxygen (dry mixing ratio q_{O_2}) and water vapor $\left(q_{H_2O}\right)$, atmospheric pressure (P), atmospheric temperature (T), line strength of the absorption line of interest (S_o) at standard temperature (T_o), the ground-state energy of the transition (ϵ), the absorption line shape (Λ) and the following universal constants: Boltzmann's constant (k_B), Planck's constant (h), and the speed of light in vacuum (c). While Eq. (7) is transcendental, temperature can be determined using a rapidly converging iterative approximation defined in Eq. (8).

$$T_{i+1} = \frac{\frac{\epsilon hc}{k_B}}{\ln\left\{\frac{T_o}{k_B} S_o \exp\left[\frac{\epsilon hc}{k_B T_o}\right] q_{O_2}\left[1 - q_{H_2O}\right]\Lambda\left(T_i\right)\right\} - \ln\left[\frac{\alpha T_i^2}{P}\right]} \tag{8}$$

5. Temperature measurement examples

With measurements of water vapor number density, backscatter ratio, and temperature-sensitive absorption of O_2, atmospheric temperature can be retrieved. The design presented in Section 3 is capable of making all such measurements. To evaluate the performance of this system, co-located comparisons are first presented to verify the accuracy of the water vapor number density and backscatter ratio, then all data are combined to demonstrate the first DIAL based temperature measurements with useful accuracy.

The MPD system described in Section 3 has been deployed in two configurations for this work to verify both ancillary data quality and test retrievals of atmospheric temperature. First, five MPD systems were co-located to compare water vapor and backscatter ratio retrievals of the system described in Section 3 with previously established and validated MPD systems. This comparison was performed specifically to quantitatively assess the retrievals from MPD systems with modular additions. Second, the system described in Section 3 was deployed to the Atmospheric Radiation Measurement (ARM) program Southern Great Plains (SGP) facility with co-located radiosonde launches and Raman lidar system to compare temperature retrievals to established techniques.

Optics EXPRESS

5.1. Water vapor and aerosol comparisons

All five of NCAR's MPD systems were deployed co-located within 80 m, housed within individual containers used for field deployment. These containers are 1.80 meters x 0.86 meters x 1.49 meters, contain all the optical components as well as the electrical and thermal control infrastructure needed for field deployment, and run off of approximately 2 kW (of which approximately 15% is used for the instrument and 85% for thermal control). All five systems had the ability to measure water vapor. Three systems, labeled MPD 1 (WV), MPD 3 (WV) and MPD 4 (WV), are water vapor DIAL systems as described by Spuler et al. [36]. One system, labeled MPD 2 (WV-HSRL), is a combined water vapor DIAL system and RbD_2 HSRL system described by Hayman and Spuler [48]. The final system, labeled MPD 5 (WV-HSRL-O_2), is as described in Section 3. Block diagrams for MPD 1-4 are given in the Appendix B for reference. All water vapor(HSRL) measurements have 5(1) min temporal resolution with 75(37.5) m range resolution, respectively. The comparison data presented here are given from a 5.5-day period from April 5th to April 10th, 2019 measured at NCAR in Boulder. This period was marked by generally clear air conditions with some high clouds present throughout the test.

Water vapor comparison leverages the extensive validation study performed by Weckwerth et al. on the NCAR water vapor DIAL [37]. Note that MPD 1 (WV) was used in this study. The water vapor(HSRL) data from the MPD systems were analyzed from 450(300) m to 6(12) km with all possible comparisons shown in Fig. 3 (4) for water vapor (backscatter ratio), respectively. Two-dimensional histograms are presented for each possible system to system comparison. Both raw signals and the water vapor absolute humidity are compared in Fig. 3, while the backscatter ratio is compared in Fig. 4. The raw signals are given as relative backscatter (RB), which is the range corrected and background subtracted water vapor offline signal with arbitrary units. Water vapor is given with units of g/m^3. Backscatter ratio is unitless. Note that here and throughout this work, colorbars are chosen to be unique to a single measurement type.

These comparisons indicate a number of conclusions. The first is that modular additions of HSRL and O_2 DIAL, as well as general alignment and optical efficiencies, can affect the raw signal levels of water vapor DIAL, i.e. raw on- and offline signals have different observed signal and noise count rates. This is expected based on the addition of optical components in the transmitter/receiver. MPD 1 (WV) and 2 (WV-HSRL) have the weakest overall signals with MPD 3 (WV) having the strongest. The second conclusion is that this RB difference is unimportant to the water vapor measurements. Best fit lines were calculated using a least squares method for the water vapor data to quantitatively evaluate this conclusion. The slopes of these lines vary from 0.96 to 1.01 with errors ranging from 4×10^{-4} to 6×10^{-4}. The correlation coefficient ranges from 0.88 to 0.95 with errors ranging from 4×10^{-4} to 9×10^{-4}. One of the major strengths of the DIAL technique is that the raw signal level is relatively unimportant to the final measurement assuming it is above minimum SNR level. The RB differences primarily drive the data availability, where higher SNR allows more data.

Similarly, best fit lines were calculated for the HSRL retrievals that show highly correlated behavior. The slope of HSRL line is $0.987 \pm 9 \times 10^{-4}$ with a correlation coefficient of $0.86 \pm 6 \times 10^{-4}$. From this comparison, we ultimately conclude that adding HSRL or additional O_2 DIAL measurements does not affect the accuracy of the water vapor measurements. Furthermore, the choice of atomic blocking filter, whether RbD_2 or KD_1, does not affect data quality assuming similar laser spectral purity and receiver atomic absorption characteristics. This is expected and confirmed on every time scale we have analyzed from hours to weeks.

5.2. Temperature measurements

The first measurements of atmospheric temperature were taken at the ARM Program's SGP facility from April 19^{th} – 22^{nd}, 2019. A 63 hour window, starting at 22 UTC on April 19^{th} and ending at 13 UTC on April 22^{nd}, of mostly clear air lacking low, optically thick cumulus and status

Optics EXPRESS

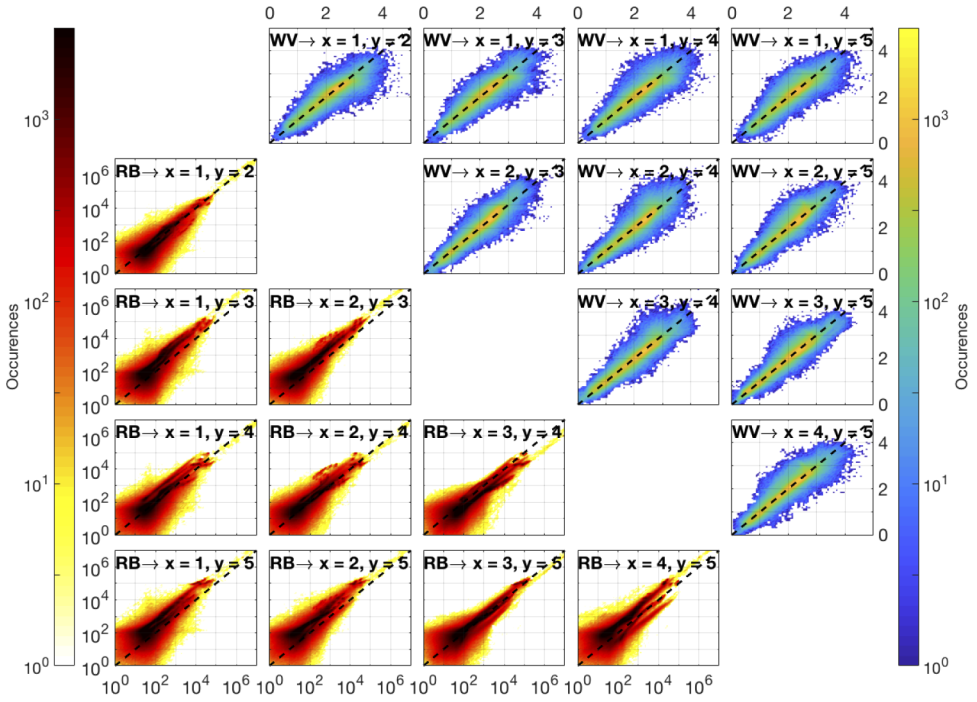

Fig. 3. 2-dimensional histogram comparisons of relative backscatter and water vapor measurements from April 5^{th} – 10^{th}, 2019 made with co-located MPD systems. MPD Systems 1-5 were used for this test with system number and axis indicated in each panel. Relative backscatter (RB) is the range corrected water vapor offline signal with arbitrary units. Water vapor (WV) is in units of g/m^3. Black dashed lines indicate 1:1 correspondence. Both colorbars are logarithmic occurrence frequency with the same bounds. All X and Y-axes are square. Note that forked RB structures, for example seen in RB comparison on MPD 4 (WV) and MPD 5 (WV-HSRL-O_2), are a result of minor realignments causing increased signal strength. No such structure is observed in the WV as it is a differential measurement.

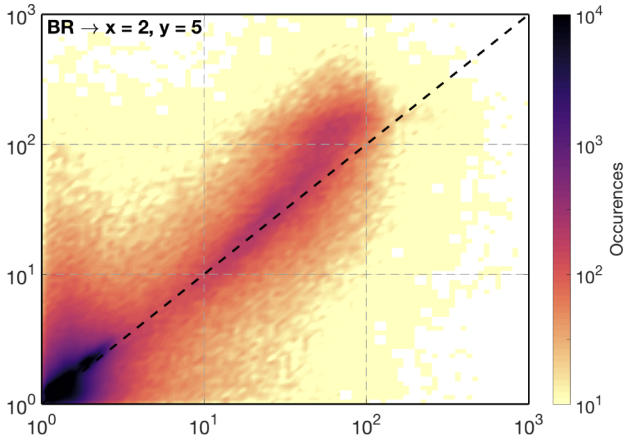

Fig. 4. Same as Fig. 3 with backscatter ratio measurements. Note that the slight drift above the 1:1 line of the data at backscatter ratio over 50 indicate a difference in output laser spectral purity.

Optics EXPRESS

clouds was chosen. The described MPD system (MPD 5 (WV-HSRL-O_2)) was deployed near a continuously running Raman lidar system [17] (approximately 60m separation) and radiosonde launch site (approximately 200m separation). The top of the boundary layer occurs between approximately 1-1.5 km over the time period with several lofted aerosol layer appearing on the third day (April 21st or 26 to 50 hours).

For this period, raw MPD data were processed as summarized in Table 2. Water vapor(backscatter ratio) data were processed at 5(1) minute and 150(75) meter resolution, respectively. These data were used as inputs to the perturbative retrieval yielding a resolution of the temperature data of 30 minutes and 225 meters. No external calibration was used for the MPD data. For comparison, Raman lidar data were taken and processed using a standard retrieval method, e.g. using Eq. (10.27) from Behrendt [41], using co-located radiosondes for calibration. The resolution of the resulting Raman temperature data is 10 minutes and 30 meters. Both DIAL and Raman temperature measurements are given in Fig. 5 as well as the KD_1 HSRL data. Over this time period, 11 radiosondes were also launched, indicated on Fig. 5 as sloped black lines, in 6 hour intervals.

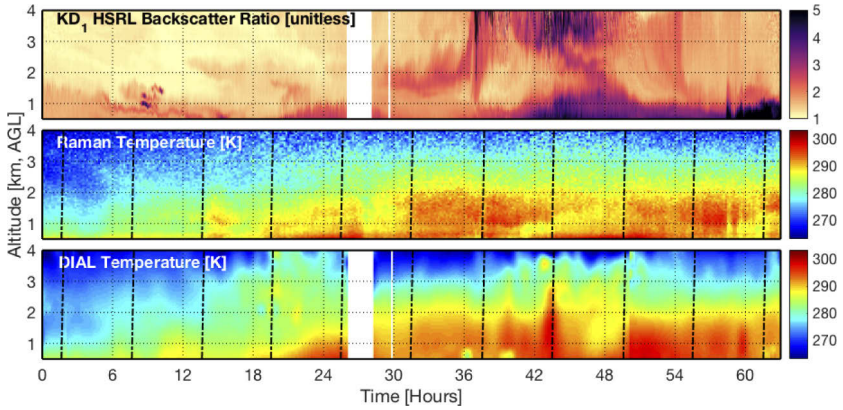

Fig. 5. Temperature and aerosol measurements from MPD and co-located Raman lidar system from April 19th – 22nd, 2019. Sloped black dashed lines indicate the time-height of co-located radiosondes. All available MPD data is presented. Data missing from the MPD system at the start of the second day are due to a software failure. Note comparisons of specific structures are given in Section 6.2.

Comparisons similar to that presented in Figs. 3 and 4 can be made between the DIAL and Raman temperature measurements as well as the DIAL and radiosonde measurements. These are presented in Figs. 6(a) and (b) for all data between 0.5km and 4.0km for the Raman(radiosonde) data with all data interpolated to the resolution of the Raman(radiosonde) data grid, respectively. The slope of the best fit line and correlation for the comparison between DIAL and Raman lidar are $1.00 \pm 1.5 \times 10^{-4}$ and $0.91 \pm 2.3 \times 10^{-3}$, respectively, and between the DIAL and radiosondes are $1.01 \pm 5.9 \times 10^{-3}$ and $0.93 \pm 3.2 \times 10^{-3}$, respectively.

To quantitatively evaluate the performance of the temperature measurements, we use the World Meteorological Organization's (WMO) requirements for global high resolution numerical weather prediction (High Res NWP) for the lower troposphere as a guide for accuracy and resolution requirements [57]. For the troposphere, a threshold(breakthrough) temperature accuracy of 3 K (1 K) is specified with temporal resolution of 6 hours (60 minutes), and a vertical resolution of 1 km (0.25 km), respectively. The breakthrough requirement for both temporal and vertical resolutions are met by the measurements presented. The accuracy requirement is evaluated using both co-located radiosondes and the co-located Raman lidar system, which has been calibrated from co-located radiosondes, as a benchmark. Note that no calibration is performed for the

Optics EXPRESS

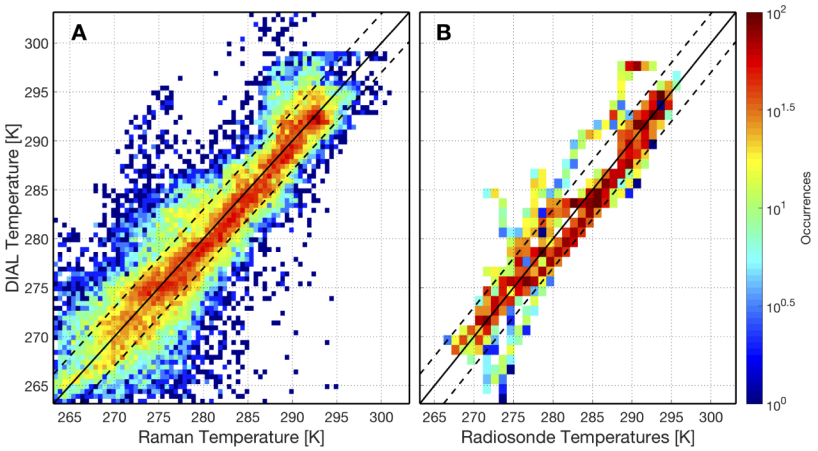

Fig. 6. Two-dimensional histogram comparisons of temperature measurements made with all available co-located MPD, Raman lidar, and radiosondes systems from April 19^{th} – 22^{nd}, 2019. The black solid line indicates 1:1 correspondence with the black dashed lines indicating the WMO threshold temperature accuracy for the lower troposphere for global High Res NWP [57]. The resolution, selected to match both histograms' colorbar values, for the Raman comparison is $0.5K$ by $0.5K$ and $1.0K$ by $1.0K$ for the radiosonde comparison.

MPD measurements. For altitudes of 0.5 *km* to 2 *km*, 79%(35%) of the data fall within the threshold(breakthrough) requirements, respectively. For altitudes of 0.5 *km* to 4 *km*, 69%(29%) of the data fall within the threshold(breakthrough) requirements.

6. Discussion

6.1. Design

With this initial proof-of-concept demonstration of a MPD system capable of measuring temperature in the O_2 A-band, a number of important design choices, compromises, and open questions remain, which should be further described and investigated. The first major choice is the selection of O_2 as an absorbing gas compared to another homogeneously mixed gas such as nitrogen (N_2). N_2 is more abundant in the atmosphere and as such might seem like a better, or more flexible, candidate for a temperature measurement than O_2. However, N_2 has no absorption lines in the wavelength range achievable with diode lasers, or indeed most of the visible and near infrared range, and as such is not useful for DIAL measurements.

Another choice to describe is the use of the KD_1 HSRL filter, which is a compromise that was carefully considered. A second viable option would be to use a dedicated pair of lasers for O_2 DIAL and a standalone RbD_2 HSRL. This would result in a 5 laser, 4 detector design compared to the presented 4 laser, 3 detector design. The major benefit of using the KD_1 HSRL is simplicity. The detriments are operational in nature. For a given cell temperature and cell length, KD_1 has lower absorption coefficient than RbD_2 (resulting mostly from lower vapor pressure [58]) and also has a broader absorption line. Practically, this means that a KD_1 HSRL cell must be hotter and has lower transmission efficiency than the comparable RbD_2 HSRL cell. Additionally, by interleaving the on- and offline wavelengths, the HSRL signal of the system presented in Fig. 1 is reduced by a factor of 2 compared to a stand alone HSRL. Furthermore, interleaving the on- and offline wavelengths requires the light from the seed laser to pass through more components with non-unity efficiency, making it more difficult to deliver adequate seed power to the amplifiers to ensure sufficient spectral purity. Finally, the optical components, currently available from commercial vendors, needed for the RbD_2 HSRL operating at 780 *nm* are slightly more mature

Optics EXPRESS

than those operating at 770 *nm*. The seed lasers and amplifiers offer slightly more power and efficiency at 780 *nm*. Considering all of these benefits/detriments, the simplicity of the design was judged paramount for this application, but different configurations (such as the 5 laser, 4 detector system) measuring similar parameters might provide better overall performance.

An additional design consideration is the specific absorption line selected. There are a number of O_2 absorption lines in the O_2 A-band that have absorption characteristics that make them viable for DIAL measurements. At minimum, O_2 absorption lines at 768.4870 *nm*, 769.2333 *nm*, 769.7958 *nm*, and 770.5878 *nm* appear to be viable choices. All these lines have slightly different maximum absorption cross-sections and temperature sensitivity. It remains an open question if there is a line that is optimum. Here, the 769.7958 *nm* has been selected for a number of practical reasons related to design simplicity. First, it is the closest available line to the KD_1 line. This allows for the narrowest interference filters, which ultimately reduces solar background noise in the O_2 DIAL measurement. Additionally, the two-component DIAL equation requires the on- and offline wavelengths to be narrowly spaced. The selected line allows for this assumption to be the best justified of all the other chosen lines. Second, the proximity of the 769.7958 *nm* O_2 line and the KD_1 line allows for the uses of adjacent etalon cavity modes, i.e. an etalon of reasonable thickness can be produced to pass both wavelengths. Other lines selected further away from the KD_1 line would require a higher free-spectral range, which would make the etalon thinner. Alternatively, using a thicker etalon would be possible in non-adjacent cavity modes, which would again result in higher solar background noise. A second viable alternative is the use of multiple etalons with different free spectral ranges that align only at the wavelengths of interest. This was considered but ultimately adds complexity, which was considered detrimental to the viability of this design. It is possible that better performance is achievable with a different absorption line than the one selected with a modification to the presented optical design. Further investigation is required to determine the optimal line and hardware configuration for temperature measurements. The given design is simply one possibility with advantageous parameters.

6.2. Performance

To analyze the performance of this proof-of-concept system, deviations of the DIAL based temperature measurements from Raman based temperature measurements (*DIAL* − *Raman*) are shown in Fig. 7. Figure 7 is constructed such that temperature measurements within the WMO threshold requirement for High Res NWP appear in white, with warmer(cooler) temperatures in red(blue), respectively. This figure specifies the Raman-based temperature measurements as its reference. Additionally, the background count rate, ($B(\lambda, \nu)$ from Eq. (1)) is given as a function of time.

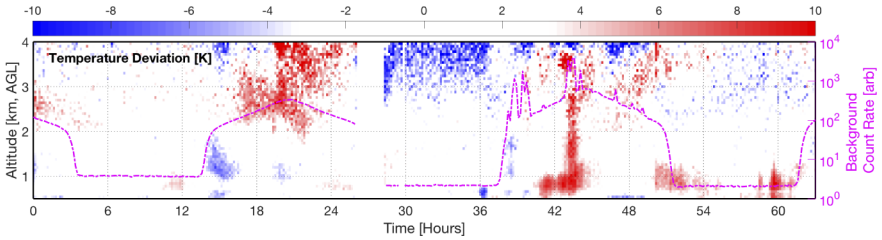

Fig. 7. Difference between DIAL and Raman lidar temperature contours (DIAL - Raman). The WMO threshold temperature range is shaded white with warmer(cooler) temperatures red(blue). Background count rate is given from the $N_{Mol}^{O_2Off}$ channel but is a good proxy for all 4 measurements near 770 *nm*.

There are a few features that clearly appear in Fig. 7 that warrant further exploration. First, while several large temperature deviations are observed, none are correlated with aerosol gradients, such

Optics EXPRESS

as the top of the boundary layer or lofted aerosol layers. The aerosol contour is provided in Fig. 5 to demonstrate this point. This lack of correlation of DIAL based temperature measurements with aerosol structure is a major advance that is possible because of the combination of DIAL and HSRL measurement that the MPD architecture readily allows. We have analyzed the data collected both with and without aerosol corrections (not shown), i.e. only using a 0^{th} order retrieval or including 1^{st} and 2^{nd} order retrieval terms as defined by Bunn et al. [55]. Uncorrected, these strong aerosol gradients can cause temperature errors in excess of 25 K. We conclude that, while aerosol corrections are necessary to measure temperature with a narrowband DIAL operating on a single line in the O_2 A-band (definitively specified by Bösenberg [40]), corrections based on quantitative measurements of aerosol structure provide superior performance than corrections based on non-quantitative methods such as Klett/Fernald inversions.

Two other errors can be understood based on the requirement of high signal-to-noise (SNR) measurements using DIAL systems. First, daytime operations appear to have less altitude range than nighttime operations. This is expected based on background noise rates. This is seen between approximately 17-22 hours, i.e. mid-day when the sun is high enough to be seen by the system. At this time, measurements above approximately 2.5km suffer higher errors than those below. Second, the major warm patch occurring from approximately 44-45 hours occurs under cloudy daytime conditions (note here the clouds are not affecting the measurements directly as they occur at about 5 km but their indirect effect increasing background count rates is). This cloudy scene raises the background noise level by over an order of magnitude compared to standard daytime operations (note that this is likely an underestimate as non-linear photon counting effects are prominent at these count rates), which are themselves more than an order of magnitude higher than nighttime conditions. From this, we conclude that the initial proof-of-concept instrument shows promise to measure full diurnal atmospheric temperature in all conditions, but that further effort to reduce background count rates are required, specifically during cloudy conditions. A reduction in background count rate is achievable with a narrower etalon passband. For comparison, the etalon in the water vapor channels (which demonstrates full diurnal operations including cloudy scenes) is approximately an order of magnitude narrower than the etalon on the O_2 channels.

One further comment should be made based on the need for high SNR using DIAL. There is a misconception about (micro-pulse) DIAL that the accuracy is based on the availability of aerosols as scatterers [59]. It should be noted that aerosols provide strong (efficient) scattering (relative to molecules), which is clearly beneficial to increase SNR, but aerosols are not required. Ultimately the accuracy of the DIAL method is based on the system's ability to measure a derivative caused by the absorption of light by a specific gas embedded within noise. Therefore, the accuracy is based on a combination of the strength of the absorption cross section, the availability of absorber gas molecules, and the overall SNR. While aerosols *may* increase SNR, there is no requirement to have only aerosol scattering, as is necessary, for example, for coherent measurements of wind using lidar. Furthermore, while some increase in SNR is valuable, large increases in SNR near clouds, for example, tend to be an overall detriment to the measurements as they cause non-linear systematic issues such as non-linear photon counting, e.g. [60]. With water vapor DIAL observations, a decline in water vapor precision is often observed above the aerosol boundary layer due to the combined reduction in scattering and reduction in absolute humidity. This is not expected with temperature measurements, as O_2 is much better mixed and more readily available in the upper troposphere than water vapor.

One final error to note is observed near clouds. The time period chosen has no low cumulus or status clouds present. It is the longest such period in the current available data set. It appears that aerosol corrections using an HSRL system are accurate for aerosol layers but as the optical depth increases, the corrections become too large to be reasonably handled as perturbations (as is assumed by [55]). This is not unexpected. Further work is required to quantify a threshold, upon which, separation of thick aerosol layers and thin clouds may be based. This work has

Optics EXPRESS

demonstrated temperature measurements in dynamic aerosol layers but has sidestepped the threshold issue, as the goal of this work is to demonstrate initial temperature measurements with DIAL, which have not been previously shown.

7. Conclusion

It is expected that continuous, range-resolved measurements of atmospheric thermodynamic variables, water vapor and temperature, will increase predictive skill of severe weather forecasts. Despite this, atmospheric thermodynamic profiles have been identified as a major observational gap by a number of sources. Active optical remote sensing shows great promise to address this observational gap, but advances in technology are required. Raman lidar systems are capable of making the desired measurements, but their design is based on a fundamentally inefficient scattering mechanism, which makes these systems typically require high powered lasers, major infrastructure to operate, and external calibration. This combination of design features make Raman lidar systems poor candidates as broadly-deployed, autonomous atmospheric thermodynamic sensors. DIAL systems do not have such fundamental limitations, but temperature measurements from DIAL systems have not been previously demonstrated. In fact, it has often been assumed that temperature measurements using DIAL will not yield useful accuracy to increase forecast predictive skill.

The major obstacle to making temperature measurements using DIAL with useful accuracy is a stringent need for ancillary information. High-quality profiles of water vapor number density and backscatter ratio are prerequisite information, in addition to temperature-sensitive absorption measurements, to retrieve temperature with DIAL. Earlier investigators attempted to approximate water vapor number density and backscatter ratio, which resulted in errors on the order of $10K$. However, the advent of diode-laser-based lidar technologies shows great promise as it can be leveraged to simultaneously measure water vapor number density, backscatter ratio, and temperature-sensitive absorption in an autonomous, field-deployable, and eye-safe manner. This has prompted the reevaluation of the assumption that DIAL systems can not measure atmospheric temperature with useful accuracy.

This work has presented a proof-of-concept lidar system that has demonstrated the capability to measure atmospheric temperature using the DIAL technique and presented the theory required to analyze the data from such a system. This system simultaneously measures water vapor number density, backscatter ratio, and temperature-sensitive O_2 absorption using a combination of DIAL and HSRL techniques. The data from this system have been presented demonstrating good agreement with co-located ancillary atmospheric sensors. Temperature measurements are then shown using the acquired data processed with a perturbative retrieval of the 2-component DIAL equation. These temperature measurements are then compared to a co-located Raman lidar and radiosonde data.

Comparisons of MPD based water vapor measurements are shown to yield consistent results, irrespective of additional observations channels, i.e. HSRL and O_2 DIAL channels. Direct comparisons of all possible system to system pairs of water vapor yields best fit lines with slopes in the range 0.96 to 1.01. The correlations of each water vapor comparison range from 0.88 to 0.95. Similarly, comparisons of backscatter ratio yield a slope of 0.987 with a correlation of 0.86. From this we conclude that the necessary ancillary information is readily measurable using the MPD architecture and design presented. Comparisons of temperature measurements with DIAL, leveraging water vapor, backscatter ratio, and O_2 absorption measurements, and Raman lidar yield a best fit line slope of 1.00 with a correlation of 0.91. Similar results are found with radiosonde data with a best fit line slope of 1.01 with a correlation of 0.93. Crucially, DIAL data is processed without the need for external calibration. Further it is shown that 79% (69%) of the data presented from $0.5 - 2(4)$ km falls within the WMO threshold accuracy for atmospheric

Optics EXPRESS

temperature for high resolution numerical weather prediction. These results demonstrate that atmospheric temperature measurements using DIAL can be made with useful accuracy.

Several areas of improvement have been highlighted, which would increase the overall performance of the presented proof-of-concept measurements. Furthermore, several theoretical avenues of future research are highlighted. First, reduction in background light levels would be beneficial to system performance, especially under bright clouds. Second, further study is needed to optimize the system design, including O_2 absorption line selection and examining aerosol corrections near clouds. Finally, comparisons have been given here assuming Raman lidar system measurements are *truth*, but more effort should be devoted in the future to develop a realistic error budget for the perturbative retrieval used to give an error bound. Here we present error estimates based on ancillary measurements, but error bounds based solely on instrument and measurement information would be of greater utility.

Appendix A. Calibration of HSRL measurements

HSRL calibration parameters come from wavelength scans of the HSRL receiver and theoretical calculations of Rayleigh-Brillouin scattering [61]. One such set of scans is shown in Fig. 8. To retrieve these efficiencies, the first scan is of the full receiver without the potassium cell heater operating, i.e. at room temperature. The second scan is of the receiver with the heater operating. All relative intensities are normalized to the maximum observed intensity from each scan.

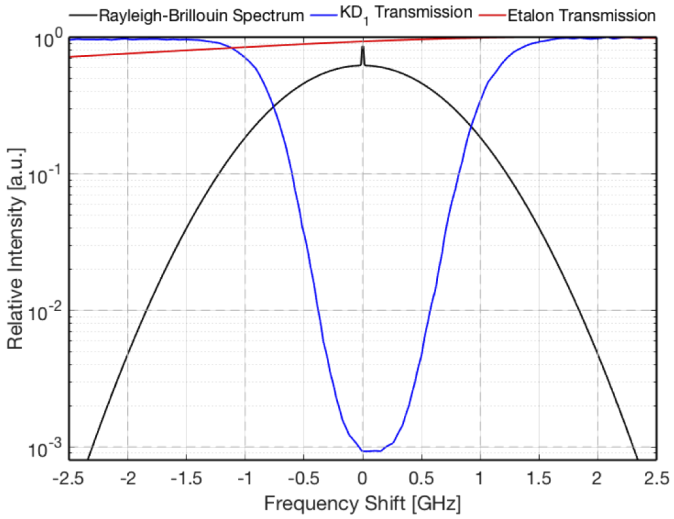

Fig. 8. Wavelength scan of etalon and KD_1 line. A theoretical Rayleigh-Brilloun backscatter spectrum, with an aerosol peak superimposed, is included [61]. The x-axis is in frequency shift from the center of the KD_1 line at 770.1085 *nm*.

The first calibration parameter, C_{MC}, accounts for the transmission of the scattered signal from molecules in the combined channel. This accounts for clipping of the molecular signal by the etalon. Rayleigh-Brillouin spectra are modeled for a wide variety of temperatures and pressures and their transmission is computed. These values are given in Fig. 9.

The second calibration parameter, C_{MM}, accounts for the transmission of the scattered signal from molecules in the molecular channel. This accounts for clipping of the molecular signal by the etalon and clipping by the KD_1 filter. Rayleigh-Brillouin spectra are modeled for a wide variety of temperatures and pressures and their transmission is computed. These values are given in Fig. 10. Here it can be seen that, while the KD_1 filter is relatively wider than a comparable filter using RbD_2, at no point does the transmission of the filter fall below 0.1 indicating that at

Optics EXPRESS

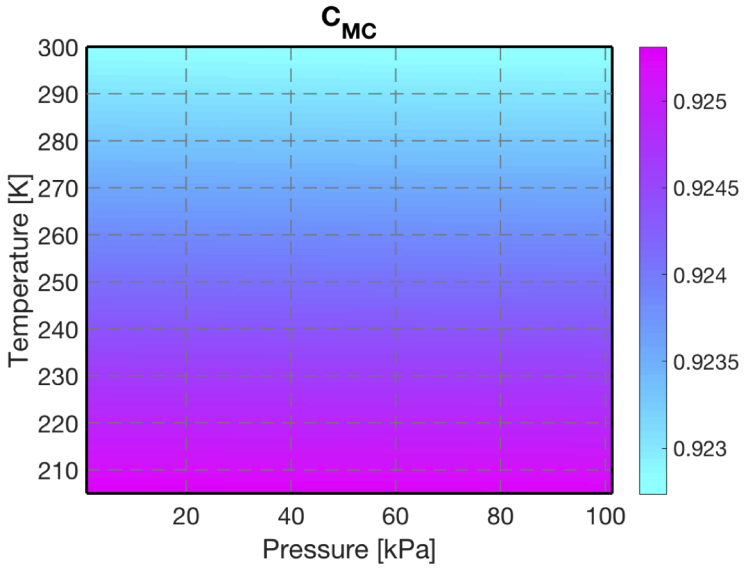

Fig. 9. Calibration parameter calculated as a function of temperature and pressure for the collection efficiency of the molecular scattered spectrum in the combined channel.

all terrestrial temperatures, the KD_1 filter can be used, i.e. there is no temperature expected to be low enough to cause the width of the KD_1 filter to result in complete attenuation of atmospheric signal.

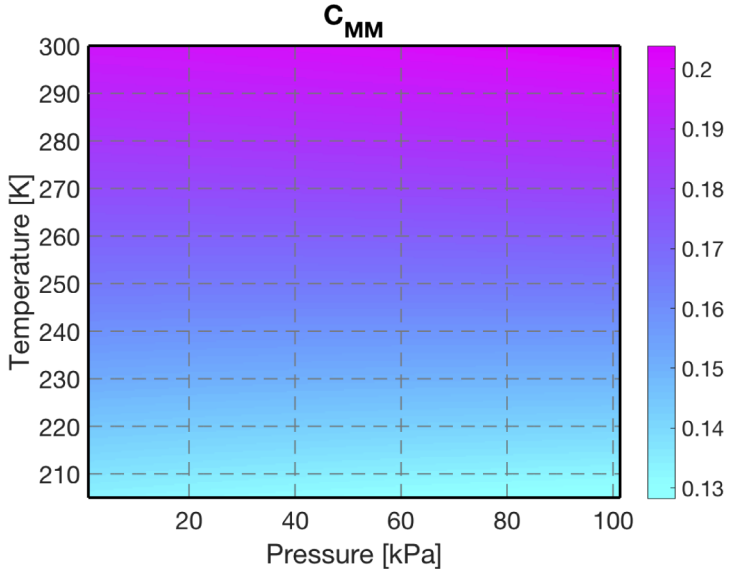

Fig. 10. Calibration parameter calculated as a function of temperature and pressure for the collection efficiency of the molecular scattered spectrum in the molecular channel.

Finally, the leakage of the aerosol scattered signal into the molecular channel can be determined from the minimum of the KD_1 absorption spectrum. In the case of the scan shown in Fig. 8, this value is $C_{AM} \approx 10^{-3}$.

Optics EXPRESS

Appendix B. MPD system block diagrams

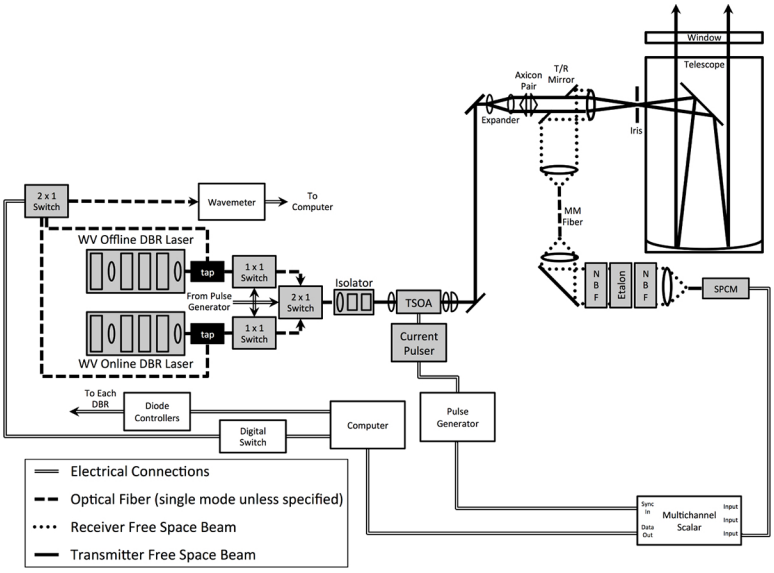

Fig. 11. A block diagram of the NCAR MPD system to measure water vapor. Abbreviations used are the same as in Fig. 1.

Block diagrams like that shown in Fig. 1 for MPD systems 1-4. MPD 1 (WV), MPD 3 (WV), and MPD 4 (WV) are water vapor DIAL systems shown in Fig. 11. MPD 2 (WV-HSRL) is a combined water vapor DIAL and RbD_2 HSRL system shown in Fig. 12.

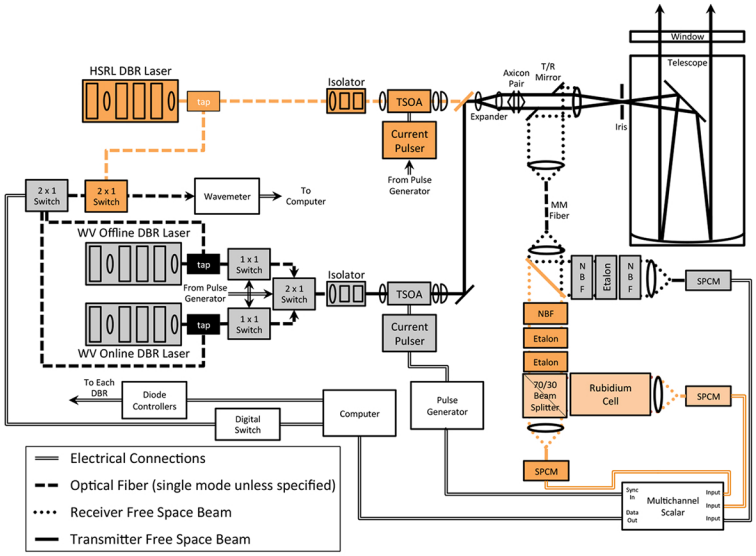

Fig. 12. A block diagram of the NCAR MPD system combining DIAL and HSRL techniques to measure water vapor and aerosol properties. Abbreviations used are the same as in Fig. 1.

Optics EXPRESS

Funding

National Science Foundation (1624736, 1852977).

Acknowledgments

This material is based upon work supported by the National Center for Atmospheric Research, which is a major facility sponsored by the National Science Foundation under Cooperative Agreement No. 1852977. The authors wish to acknowledge to contributions of the following NCAR staff who where involved in design and construction of the five MPD units used in this study: Todd Bernatsky, Rich Ericson, Josh Carnes, Brad Schoenrock, Eric Loew, Jim Ranson, and the EOL Design and Fabrication Services. The authors also wish to thank the ARM Program, Rob Newsom, and the staff of the Southern Great Plains field site for hosting the MPD instruments and providing both Raman lidar and radiosonde data. Finally, the authors would like to acknowledge Tammy Weckwerth and Holger Vömel for helpful discussions and their comments in compiling this manuscript.

Disclosures

The authors declare no conflicts of interest.

References

1. N. R. Council, *Observing Weather and Climate from the Ground Up: A Nationwide Network of Networks* (The National Academies Press, Washington, DC, 2009).
2. N. R. Council, *When Weather Matters: Science and Services to Meet Critical Societal Needs* (The National Academies Press, Washington, DC, 2010).
3. V. Wulfmeyer, R. M. Hardesty, D. D. Turner, A. Behrendt, M. P. Cadeddu, P. Di Girolamo, P. Schlüssel, J. Van Baelen, and F. Zus, "A review of the remote sensing of lower tropospheric thermodynamic profiles and its indispensable role for the understanding and the simulation of water and energy cycles," Rev. Geophys. **53**(3), 819–895 (2015).
4. N. A. of Sciences Engineering and Medicine, *The Future of Atmospheric Boundary Layer Observing, Understanding, and Modeling: Proceedings of a Workshop* (The National Academies Press, Washington, DC, 2018).
5. G. Placzek, "The rayleigh and raman scattering," in *Handbuch der Radiologie* (Akademische Verlagsgesellschaft, 1934), pp. 209–374.
6. J. A. Cooney, "Measurements on the raman component of laser atmospheric backscatter," Appl. Phys. Lett. **12**(2), 40–42 (1968).
7. R. D. Boudreau, "On the use of ultraviolet lidar for observing atmospheric constituents by raman scattering," J. Appl. Meteorol. **9**(2), 316–317 (1970).
8. D. A. Long, *The Raman Effect: A Unified Treatment of the Theory of Raman Scattering by Molecules* (John Wiley and Sons, Ltd, 2002).
9. D. N. Whiteman, "Examination of the traditional raman lidar technique. i. evaluating the temperature-dependent lidar equations," Appl. Opt. **42**(15), 2571–2592 (2003).
10. D. N. Whiteman, "Examination of the traditional raman lidar technique. ii. evaluating the ratios for water vapor and aerosols," Appl. Opt. **42**(15), 2593–2608 (2003).
11. D. N. Whiteman, S. H. Melfi, and R. A. Ferrare, "Raman lidar system for the measurement of water vapor and aerosols in the earth's atmosphere," Appl. Opt. **31**(16), 3068–3082 (1992).
12. A. Apituley, K. M. Wilson, C. Potma, H. Volten, and M. de Graaf, "Performance assessment and application of caeli — a high-performance raman lidar for diurnal profiling of water vapour, aerosols and clouds," in *Proceedings of the 8th International Symposium on Tropospheric Profiling*, A. Apituley, H. W. J. Russchenberg, and W. A. A. Monna, eds. (2009).
13. R. R. Neely and J. P. Thayer, "Raman lidar profiling of tropospheric water vapor over kangerlussuaq, greenland," J. Atmospheric Ocean. Technol. **28**(9), 1141–1148 (2011).
14. A. Moss, R. J. Sica, E. McCullough, K. Strawbridge, K. Walker, and J. Drummond, "Calibration and validation of water vapour lidar measurements from eureka, nunavut, using radiosondes and the atmospheric chemistry experiment fourier transform spectrometer," Atmos. Meas. Tech. **6**(3), 741–749 (2013).
15. T. Dinoev, V. Simeonov, Y. Arshinov, S. Bobrovnikov, P. Ristori, B. Calpini, M. Parlange, and H. van den Bergh, "Raman lidar for meteorological observations, ralmo – part 1: Instrument description," Atmos. Meas. Tech. **6**(5), 1329–1346 (2013).
16. E. Brocard, R. Philipona, A. Haefele, G. Romanens, A. Mueller, D. Ruffieux, V. Simeonov, and B. Calpini, "Raman lidar for meteorological observations, ralmo – part 2: Validation of water vapor measurements," Atmos. Meas. Tech. **6**(5), 1347–1358 (2013).

Optics EXPRESS

17. J. E. M. Goldsmith, F. H. Blair, S. E. Bisson, and D. D. Turner, "Turn-key raman lidar for profiling atmospheric water vapor, clouds, and aerosols," Appl. Opt. **37**(21), 4979–4990 (1998).
18. J. Reichardt, U. Wandinger, V. Klein, I. Mattis, B. Hilber, and R. Begbie, "Ramses: German meteorological service autonomous raman lidar for water vapor, temperature, aerosol, and cloud measurements," Appl. Opt. **51**(34), 8111–8131 (2012).
19. A. Cohen, J. A. Cooney, and K. N. Geller, "Atmospheric temperature profiles from lidar measurements of rotational raman and elastic scattering," Appl. Opt. **15**(11), 2896–2901 (1976).
20. Y. F. Arshinov, S. M. Bobrovnikov, V. E. Zuev, and V. M. Mitev, "Atmospheric temperature measurements using a pure rotational raman lidar," Appl. Opt. **22**(19), 2984–2990 (1983).
21. P. Di Girolamo, R. Marchese, D. N. Whiteman, and B. B. Demoz, "Rotational raman lidar measurements of atmospheric temperature in the uv," Geophys. Res. Lett. **31**(1), L01106 (2004).
22. M. Radlach, A. Behrendt, and V. Wulfmeyer, "Scanning rotational raman lidar at 355 nm for the measurement of tropospheric temperature fields," Atmospheric Chem. Phys. Discuss. **7**(3), 7569–7602 (2007).
23. D. Wu, Z. Wang, P. Wechsler, N. Mahon, M. Deng, B. Glover, M. Burkhart, W. Kuestner, and B. Heesen, "Airborne compact rotational raman lidar for temperature measurement," Opt. Express **24**(18), A1210–A1223 (2016).
24. E. Landulfo, R. F. D. Costa, A. S. Torres, F. J. S. Lopes, D. N. Whiteman, and D. D. Venable, "Raman water vapor lidar calibration," (2009).
25. D. D. Venable, D. N. Whiteman, M. N. Calhoun, A. O. Dirisu, R. M. Connell, and E. Landulfo, "Lamp mapping technique for independent determination of the water vapor mixing ratio calibration factor for a raman lidar system," Appl. Opt. **50**(23), 4622–4632 (2011).
26. M. Walker, D. Venable, D. N. Whiteman, and T. Sakai, "Application of the lamp mapping technique for overlap function for raman lidar systems," Appl. Opt. **55**(10), 2551–2558 (2016).
27. H. Van De Hulst, *Light Scattering By Small Particles* (John Wiley and Sons, 1957).
28. C. F. Bohren and D. R. Huffman, *Absorption and Scattering of Light by Small Particles* (WILEY-VCH Verlag GmbH and Co. KGaA, 1998).
29. C.-Y. She, "Spectral structure of laser light scattering revisited: bandwidths of nonresonant scattering lidars," Appl. Opt. **40**(27), 4875–4884 (2001).
30. C. F. Bohren and E. E. Clothiaux, *Fundamentals of Atmospheric Radiation* (WILEY-VCH Verlag GmbH and Co. KGaA, Weinheim, Germany, 2005).
31. S. Ismail and E. V. Browell, "Airborne and spaceborne lidar measurements of water vapor profiles: a sensitivity analysis," Appl. Opt. **28**(17), 3603–3615 (1989).
32. D. Bruneau, P. Quaglia, C. Flamant, M. Meissonnier, and J. Pelon, "Airborne lidar leandre ii for water-vapor profiling in the troposphere. i. system description," Appl. Opt. **40**(21), 3450–3461 (2001).
33. G. Poberaj, A. Fix, A. Assion, M. Wirth, C. Kiemle, and G. Ehret, "Airborne all-solid-state dial for water vapour measurements in the tropopause region: system description and assessment of accuracy," Appl. Phys. B **75**(2-3), 165–172 (2002).
34. A. R. Nehrir, K. S. Repasky, and J. L. Carlsten, "Eye-safe diode-laser-based micropulse differential absorption lidar (dial) for water vapor profiling in the lower troposphere," J. Atmospheric Ocean. Technol. **28**(2), 131–147 (2011).
35. K. S. Repasky, D. Moen, S. Spuler, A. R. Nehrir, and J. L. Carlsten, "Progress towards an autonomous field deployable diode-laser-based differential absorption lidar (dial) for profiling water vapor in the lower troposphere," Remote Sens. **5**(12), 6241–6259 (2013).
36. S. M. Spuler, K. S. Repasky, B. Morley, D. Moen, M. Hayman, and A. R. Nehrir, "Field-deployable diode-laser-based differential absorption lidar (dial) for profiling water vapor," Atmos. Meas. Tech. **8**(3), 1073–1087 (2015).
37. T. M. Weckwerth, K. J. Weber, D. D. Turner, and S. M. Spuler, "Validation of a water vapor micropulse differential absorption lidar (dial)," J. Atmospheric Ocean. Technol. **33**(11), 2353–2372 (2016).
38. M. Wirth, A. Fix, P. Mahnke, H. Schwarzer, F. Schrandt, and G. Ehret, "The airborne multi-wavelength water vapor differential absorption lidar wales: system design and performance," Appl. Phys. B **96**(1), 201–213 (2009).
39. F. A. Theopold and J. Bösenberg, "Differential absorption lidar measurements of atmospheric temperature profiles: Theory and experiment," J. Atmospheric Ocean. Technol. **10**(2), 165–179 (1993).
40. J. Bösenberg, "Ground-based differential absorption lidar for water-vapor and temperature profiling: methodology," Appl. Opt. **37**(18), 3845–3860 (1998).
41. C. Weitkamp, ed., *Lidar Range-Resolved Optical Remote Sensing of the Atmosphere*, vol. 102 (Springer, 233 Spring Street, New York, NY 10013, USA, 2005).
42. R. M. Measures, *Laser Remote Sensing: Fundamentals and Applications* (John Wiley and Sons, 6000 Broken Sound Parkway NW, Suite 300, Boca Raton, FL 33487-2742, USA, 1984).
43. T. Fujii and T. Fukuchi, eds., *Laser Remote Sensing* (Taylor and Francis Group, 2005).
44. C. L. Korb and C. Y. Weng, "A theoretical study of a two-wavelength lidar technique for the measurement of atmospheric temperature profiles," J. Appl. Meteorol. **21**(9), 1346–1355 (1982).
45. F. G. Fernald, B. M. Herman, and J. A. Reagan, "Determination of aerosol height distributions by lidar," J. Appl. Meteorol. **11**(3), 482–489 (1972).
46. J. D. Klett, "Stable analytical inversion solution for processing lidar returns," Appl. Opt. **20**(2), 211–220 (1981).
47. V. Wulfmeyer, "Ground-based differential absorption lidar for water-vapor and temperature profiling: development and specifications of a high-performance laser transmitter," Appl. Opt. **37**(18), 3804–3824 (1998).

Optics EXPRESS

48. M. Hayman and S. Spuler, "Demonstration of a diode-laser-based high spectral resolution lidar (hsrl) for quantitative profiling of clouds and aerosols," Opt. Express **25**(24), A1096–A1110 (2017).
49. R. M. Schotland, "Errors in the lidar measurement of atmospheric gases by differential absorption," J. Appl. Meteorol. **13**(1), 71–77 (1974).
50. P. Piironen and E. W. Eloranta, "Demonstration of a high-spectral-resolution lidar based on an iodine absorption filter," Opt. Lett. **19**(3), 234–236 (1994).
51. A. Ansmann, U. Wandinger, M. Riebesell, C. Weitkamp, and W. Michaelis, "Independent measurement of extinction and backscatter profiles in cirrus clouds by using a combined raman elastic-backscatter lidar," Appl. Opt. **31**(33), 7113–7131 (1992).
52. L. Rothman, I. Gordon, Y. Babikov, A. Barbe, D. C. Benner, P. Bernath, M. Birk, L. Bizzocchi, V. Boudon, L. Brown, A. Campargue, K. Chance, E. Cohen, L. Coudert, V. Devi, B. Drouin, A. Fayt, J.-M. Flaud, R. Gamache, J. Harrison, J.-M. Hartmann, C. Hill, J. Hodges, D. Jacquemart, A. Jolly, J. Lamouroux, R. L. Roy, G. Li, D. Long, O. Lyulin, C. Mackie, S. Massie, S. Mikhailenko, H. Müller, O. Naumenko, A. Nikitin, J. Orphal, V. Perevalov, A. Perrin, E. Polovtseva, C. Richard, M. Smith, E. Starikova, K. Sung, S. Tashkun, J. Tennyson, G. Toon, V. Tyuterev, and G. Wagner, "The hitran2012 molecular spectroscopic database; HITRAN2012 special issue," J. Quant. Spectrosc. Radiat. Transfer **130**, 4–50 (2013).
53. U. von Zahn and J. Höffner, "Mesopause temperature profiling by potassium lidar," Geophys. Res. Lett. **23**(2), 141–144 (1996).
54. M. Hayman, R. A. Stillwell, and S. M. Spuler, "Fast computation of absorption spectra for lidar data processing using principal component analysis," Opt. Lett. **44**(8), 1900–1903 (2019).
55. C. E. Bunn, K. S. Repasky, M. Hayman, R. A. Stillwell, and S. M. Spuler, "Perturbative solution to the two-component atmosphere dial equation for improving the accuracy of the retrieved absorption coefficient," Appl. Opt. **57**(16), 4440–4450 (2018).
56. K. S. Repasky, C. E. Bunn, M. Hayman, R. A. Stillwell, and S. M. Spuler, "Modeling the performance of a diode laser-based (dlb) micro-pulse differential absorption lidar (mpd) for temperature profiling in the lower troposphere," Opt. Express **27**(23), 33543–33563 (2019).
57. "Observing systems capability analysis and review tool," (2019).
58. R. K. Hanley, P. D. Gregory, I. G. Hughes, and S. L. Cornish, "Absolute absorption on the potassium d lines: theory and experiment," J. Phys. B: At., Mol. Opt. Phys. **48**(19), 195004 (2015).
59. K. R. Haghi, B. Geerts, H. G. Chipilski, A. Johnson, S. Degelia, D. Imy, D. B. Parsons, R. D. Adams-Selin, D. D. Turner, and X. Wang, "Bore-ing into nocturnal convection," Bull. Am. Meteorol. Soc. **100**(6), 1103–1121 (2019).
60. D. P. Donovan, J. A. Whiteway, and A. I. Carswell, "Correction for nonlinear photon-counting effects in lidar systems," Appl. Opt. **32**(33), 6742–6753 (1993).
61. G. Tenti, C. D. Boley, and R. C. Desai, "On the kinetic model description of rayleigh–brillouin scattering from molecular gases," Can. J. Phys. **52**(4), 285–290 (1974).